This is the pre-peer reviewed version of the following article:
T. Katase, K. Endo, T. Tohei, Y. Ikuhara, and H. Ohta, Advanced Electronic Materials 1, 1500063 (2015)., which has been published in final form at http://onlinelibrary.wiley.com/wol1/doi/10.1002/aelm.201500063/abstract.

Room-temperature-protonation-driven on-demand metal-insulator conversion of a transition metal oxide

Takayoshi Katase[1,*], Kenji Endo[1], Tetsuya Tohei[2], Yuichi Ikuhara[2], and Hiromichi Ohta[1,*]

[1]Research Institute for Electronic Science, Hokkaido University, N20W10, Sapporo 001-0020, Japan

[2]Institute of Engineering Innovation, The University of Tokyo, 2-11-16 Yayoi, Bunkyo-ku, Tokyo 113-8656, Japan

[*]E-mail: katase@es.hokudai.ac.jp, hiromichi.ohta@es.hokudai.ac.jp

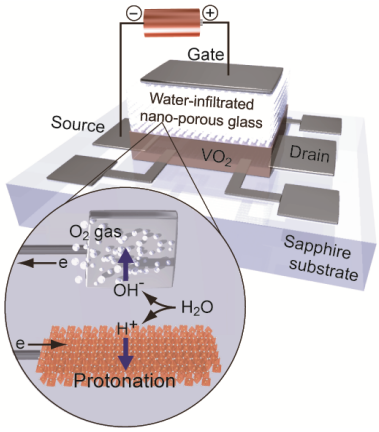

Room-temperature protonation and metal-insulator conversion of a transition metal oxide (TMO) was demonstrated by all-solid-state thin-film transistor with vanadium dioxide using a water-infiltrated nanoporous glass as a solid electrolyte. This promising result can provide a novel route for TMO-based solid-state electro-optical devices, in particular, smart windows for on-demand infrared shielding.

Keywords: protonation, solid state electrochemistry, transition metal oxide, thin film transistor

Hydrogen in transition metal oxides (TMOs) commonly exist as protons (H^+) through covalent O-H bonding with the surrounding oxide ions (O^{2-})[1] and act as shallow donors that donate an electron to TM cations,[2] resulting in a dramatic change in the electro-optical properties.[3] Although H^+ has historically been viewed as the most ubiquitous impurity,[4] recent studies suggest that it may reveal the potential characteristics in TMOs. Protonation of TMOs is the most ideal technique to modulate their functions, even as compared with state-of-the-art modulation techniques,[5,6] due to their intrinsic nonvolatile operation,[7,8] but protonation is not typically utilized for solid-state devices because of imperative high-temperature annealing treatment in hydrogen source. Although one solution for room temperature (RT) protonation of TMOs is liquid-phase electrochemistry through electrolysis of an aqueous solution, which has been a facile method to protonate TMOs at RT,[9,10] it is unsuited for practical purposes due to liquid-leakage problem. Hence, protonation/deprotonation in solid-state devices has yet to be realized in practical applications.

Herein, we focus on vanadium dioxide (VO_2) to demonstrate solid-state protonation and conversion of the electronic states from an insulator to a metal at RT. VO_2 is classically well-known thermochromic TMO, which shows metal-insulator (MI) transition at the transition temperature (T_{MI}) of 68 °C.[11] The MI transition accompanies a structural change from a low-temperature monoclinic to a high-temperature tetragonal (rutile-type) structure, which causes reconstruction of electronic structures to open up a charge gap of ~0.6 eV,[12] resulting in the abrupt change of electrical and optical properties at the MI transition. In particular, the dramatic change of optical transmittance in infrared region while maintaining visible transparency has potential for heat-blocking smart window, which enables us to intelligently regulate and utilize sunlight, leading to energy saving in architectures. These features of VO_2 offer several advantages compared to visible-color switching of conventional

electrochromic devices. However, the relatively high T_{MI} of VO_2 makes it awkward to use at appropriate temperatures for practical applications.

Protonation of VO_2 (H_xVO_2) is one of the effective ways to reduce T_{MI} and modulate the electronic state from an insulator to a metal via hydrogen spillover through thermal annealing of the VO_2 nanobeam in H_2 / vacuum conditions.[13] MI phase modulation has also been achieved by electrostatic-charge doping with ionic-liquid-gated transistors[14,15] and epitaxial strains in thin films,[16] but protonation of VO_2 via a chemical route is the most ideal to engineer the MI transition characteristics due to the intrinsic non-volatile operations similar to a conventional electrochromic device based on H_xWO_3.[3] However, protonation of VO_2 requires a high-temperature heat treatment,[17–19] and the uptake of H^+ into VO_2 was extremely slow at RT, *i.e.* the chemical solubility of H_xVO_2 was very small at $x = 0.08$.[17] Controlling the MI phase transition by RT protonation has technological importance as a step toward practical uses.

Here we propose a new solid-state device for on-demand-protonation of VO_2 thin films at RT using a thin film transistor (TFT) combined with water-electrolysis.[20] **Figure 1**a schematically illustrates the device structure of a water-electrolysis TFT composed of water-infiltrated nanoporous glass as a gate insulator, which serves as solid electrolyte.[20] The gate insulator consists of an amorphous $12CaO{\cdot}7Al_2O_3$ (a-C12A7) thin film with nanoporous structure (Hereafter this film is abbreviated as CAN). C12A7 is hydroscopic material, and water vapor in air is automatically absorbed into the CAN film due to the capillary effect of the interconnected nanopores.[20] A gate bias application induces water electrolysis in the CAN gate insulator, and produced electro-active H^+ (H_3O^+) and OH^- ions can be used to protonate and deprotonate the VO_2 channel layer, respectively. The water-electrolysis TFT can be considered as a nanosized electrochemical cell that enables reversible

protonation/deprotonation in a high-electric field. Consequently, the ~10-nm-thick VO_2 layer was reversibly altered from an insulator to a metal by changing the external gate voltage up to 35 V at RT. The protonation was clearly accompanied by the structural change from monoclinic VO_2 to tetragonal H_xVO_2 phase. The MI phase modulation in protonated VO_2 under an applied voltage at RT offer a new route to all-solid-state smart windows for on-demand infrared shielding, and the present results lead to a universal approach to modulate the electrical and optical properties of TMOs via water-electrolysis-induced protonation.

The TFT structure was fabricated on 20-nm-thick VO_2 epitaxial films (channel size: 800-μm long and 400-μm wide) grown on $(11\bar{2}0)$ sapphire substrates by pulsed laser deposition. Crystallographic characterization of the VO_2 epitaxial film is summarized in Figure S1 in Supporting Information. T_{MI} of as-grown VO_2 films was 65 °C, which is similar to 68 °C of bulk VO_2.[11] Figure 1b shows an optical micrograph of the VO_2-based water-electrolysis TFT. Metallic Ti films were used for Source (S), Drain (D) and Gate (G) electrodes. A 200-nm thick CAN film was used for a gate insulator as solid electrolyte, where the film was deposited at RT under an oxygen pressure of 5 Pa to realize a nanoporous structure. (The relative density of the CAN film was 71 % with respect to 2.92 g cm^{-3} of a dense C12A7 film).[20] Figure 1c shows Z-contrast, high-angle, annular dark-field scanning transmission electron microscope (HAADF-STEM) image of the cross-sectional TFT structure. The numerous dark spots with 10–20 nm diameters indicate that the high-density nanopores were incorporated in the CAN film. For the protonation of VO_2 by water-electrolysis TFTs, we focused on the electronic structure of parent (insulating) VO_2. The energy-band diagram of VO_2[21] with respect to the electric potentials of oxidation and reduction of H_2O (Figure S2 in Supporting Information) shows that the conduction band minimum is below the electric potential of cathode reaction ($2H^+ + 2e^- \rightarrow H_2$) and the valence band maximum is above that of anode reaction ($H_2O \rightarrow 1/2O_2 + 2H^+ + 2e^-$). Thus, the proton

can be expected to move into and get out from VO_2 channel layer without the gas generation by applying positive and negative electric-fields, respectively.

VO_2-based water-electrolysis TFTs were characterized at RT by measuring sheet resistance (R_s) and thermopower (S) after applying and subsequently switching off gate bias. It should be noted that S-values can be used to easily evaluate the metal-insulator conversion because they basically reflect the energy differential of density of state at Fermi energy and are sensitive to significant changes in the electronic structure of VO_2 at T_{MI}.[22] **Figures 2**a and b plot the gate voltage (V_g) dependence of R_s and S-values at RT for VO_2-based water-electrolysis TFTs, respectively. The dependence was measured immediately after the bias application for 10 minutes at each positive voltage from +5 V to +35 V. A double-digit decrease in R_s from the virgin state (68 kΩ sq^{-1}) to 0.5 kΩ sq^{-1} at +35 V was clearly observed, and the R_s continued to decrease by positive V_g application. Meanwhile, $|S|$-value drastically decreased form 200 μV K^{-1} of insulating parent VO_2 phase[22] as the positive V_g increased up to +30 V and became saturated at 43 μV K^{-1}, which is close to that of metallic H_xVO_2 bulk (~35 μV K^{-1}). [19] These results are discussed by comparing the electronic structures of insulating H_xVO_2 ($T < T_{MI}$) and metallic H_xVO_2 ($T > T_{MI}$). Schematic electronic structures around Fermi energy are shown in Figure S3 in Supporting Information. H^+ doping into insulating H_xVO_2 provides electrons to the conduction band, and the gradient of DOS becomes moderate, resulting in the consequent reduction of $|S|$-values. On the other hand, $|S|$-values of metallic H_xVO_2 are constant at ~35 μVK^{-1} at $T > T_{MI}$. Therefore, the decrease in $|S|$-values and their saturation as V_g increases reflect a change in the electronic state from an insulator to a metal. The inset in Figure 2a summarizes the V_g dependence of I_g during the bias application at each V_g. Although I_g at V_g = +5 V was small bellow 10 pA, I_g exponentially increased with respect to V_g from +10 V to +35 V, suggesting that I_g originates from the ion current of water-electrolysis in the CAN film and electrochemical reaction of VO_2 film.

These findings suggest the device operation mechanism as follows. First, V_g application at +5 V accumulates charge carriers at the VO_2 film surface via a pure electrostatic field effect due to the negligible leakage current, resulting in the formation of parallel-plate capacitor (*i.e.* the electric field starts to be well applied on the surface of VO_2 channel). Using a capacitance (C) of 160 pF for the CAN gate insulator,[20] the accumulated sheet carrier density is estimated to be 1.6×10^{12} cm^{-2} at V_g = +5 V. A further gate bias application generates dissociated H^+ and OH^- ions in the solid gate insulator, which are attracted to the surface of VO_2 and Ti, respectively. H^+ ions penetrate into the VO_2 crystal (H_xVO_2), while OH^- ions form an oxidized TiO_2 passivation layer on the Ti film surface or become O_2 gas at the interface, where the electrostatic potential with linear distribution should be formed across CAN layer. Therefore, threshold voltage of the device operation for the water-electrolysis TFTs can be considered to be much higher than the H_2O dissociation potential of 1.23 V. The high electric field formed in the nanosized electrochemical cell should achieve RT protonation of the VO_2 thin film, as illustrated in Figure 1a. It should be noted that the protonated VO_2 film is stable under ambient and vacuum conditions at RT. The retention time dependence of R_s monitored after switching the gate bias (+20 V) off is shown in Figure S4a in Supporting Information. Although slight decrease of R_s was observed in air, R_s are almost persistent following the removal of V_g, confirming the non-volatility of device operation due to the chemical reaction.

Then, we performed reversible operation of VO_2-based water-electrolysis TFTs, *i.e.* protonation and deprotonation by changing positive and negative gate bias. Figure 2c shows the temperature dependences of R_s before and after applying V_g alternately at +20 V and –20 V at RT, where R_s–T was measured after switching off V_g. The inset plots logarithm of R_s versus T to show the MI transition clearly. R_s–T were reversibly modulated and recovered to

initial state, where the ON/OFF ratio was ~30 at RT. However, unlike the previous report on bulk H_xVO_2,[13] T_{MI} did not shift to lower temperature and was almost unchanged.

Considering that the R_s continues to decrease as V_g increases and the $|S|$-values reaches at that of metal H_xVO_2 at V_g = +30 V (Figures 2a and b), only the film surface region becomes metal due to an insufficient H^+ migration from the surface into bulk region. To estimate the thickness (d) of metal H_xVO_2 layer, we used a simple bi-layer model of thermopower,[23] where the parallel circuit composed of metal (M) and insulator (I) layers was considered to calculate the combined electromotive force. (The electromotive force depends on both the conductivity and thickness of each layer.) The observed $|S|$-value ($|S|_{obsd.}$ = 43 μV K^{-1}) of the present TFTs can be expressed by the equation of $|S|_{obsd.} = (\sigma_{sM} \cdot |S|_M + \sigma_{sI} \cdot |S|_I)/(\sigma_{sM} + \sigma_{sI})$, where sheet conductance σ_{sM} and σ_{sI} are defined as $\sigma_M \times d$ and $\sigma_I \times (20-d)$, respectively. The physical properties of conductivity and $|S|$-values for the M and I phases are used from those of reported bulk H_xVO_2[19] and virgin VO_2 TFTs (Figures 2a and b), respectively. As a result, maximum thickness of metallic layer, after the V_g application at +35 V, is estimated to be 11 nm, confirming that the VO_2 film surface was changed from an insulator to a metal state.

The MI transition of VO_2 is strongly coupled with crystal structure change from an insulating monoclinic phase to a metallic tetragonal phase, which is accompanied by the disappearance of V^{4+}-ion dimer.[12] To validate the crystal structure change of protonated VO_2 film, structural analysis was performed by electron diffraction with TEM at RT. **Figures** 3a and b present the nano-beam electron diffraction (ED) patterns observed at about 5 nm in depth from surface region of VO_2 film, before (a) and after protonation (b) with an incident electron beam along the [010] direction of VO_2. The initial ED pattern (a) is consistent with the monoclinic structure, where the diffraction spots of superstructures, indicated by arrows,

originate from the formation of V^{4+}-ion dimer. Following the protonation (b), the diffraction spots due to the superstructures disappear, demonstrating a transformation from the monoclinic to the tetragonal phase (Figures 3c and d). This result indicates that crystal structure was changed by water-electrolysis-induced protonation of VO_2, which provides evidence of metal-insulator conversion. It should be noted that, for heavily-protonated H_xVO_2 nanobeams[24] and ionic-liquid-gated VO_2 TFTs,[25] their metallic phases were recently found to have the partially retained V3*d* orbital ordering. However, the pairing of V ions was not confirmed in the present ED patterns. Additional investigation is necessary to verify this inconsistency in the future.

The metal-insulator conversion must be reversibly controlled in a practical time for the application to electronic devices. **Figures** 4a and 4b present I_g under V_g application and R_s at the OFF state versus number of gate pulses of +20 V and −20 V at RT, where each pulse duration is 1 min. Upon the application of V_g within 1 min, a large I_g of ~±160 μA was observed and consequently reversible switching of R_s was realized. The voltage switching of metal-insulator conversion demonstrates great potentials ~~especially~~ for ~~on-demand-operating smart windows~~ advanced electronic devices based on protonated VO_2. Here, we like to discuss a typical time scale of the switching process and its V_g dependence of VO_2-based water-electrolysis TFTs. The switching speed of metal-insulator conversion can be considered to depend on water-electrolysis, ion migration in the solid electrolyte, and proton diffusion into VO_2 film under V_g application. In particular, the proton diffusion should limit the operation speed in this case because of the low diffusion constant of proton at RT. Therefore, the device-operation speed should strongly depend on the density of protons accumulated at the surface of VO_2 channel. Therefore, the speed of metal-insulator phase switching should basically depend on V_g, because the density of protons ($\equiv I_g$) exponentially increases with V_g.

There has been a considerable debate concerning the field-induced MI phase conversion of ionic-liquid-gated VO_2 TFTs, in which it results from a collapse of the Mott insulator due to electrostatically accumulated electrons at the film surface[14] or arises from the formation of oxygen vacancies due to an electric-field-induced oxygen migration during the gating process.[15] The latter one might be valid for CAN-gated water-electrolysis TFTs, but, in this case, the DC of I_g keeps unchanged, during V_g application, at extremely large value of 0.1–1 mA without the decay for 60 sec at least (Fig. 4(a)) and it is hard to consider the CAN forms the capacitor structure. The present device seems to operate like rechargeable Ni-H_2 battery with constant ionic current, where linear electric-field induces the penetration of ions into each electrode. Therefore, electric-field effect on VO_2 film surface should not be so high to induce oxygen vacancies in the film because of the lack of electric double layer at the interface. In addition, it is known fact that H^+ can penetrate into VO_2 crystal and H^+ with smallest ionic radii (*i.e.* just proton without electron shell)[26] is easily considered to penetrate into VO_2 crystal, compared to the large cations of ionic liquids (~10^2 pm) such as HMIM-TFSI[15] (in this case, the oxygen vacancy mechanism might work.) Therefore, protonation should tend to take place more than electric-field-induced oxygen migration in the present device.

To investigate the pure electric-field effect on this VO_2-TFT, we fabricated TFT structure with water-free gate insulator of a fully dense a-C12A7 film (*i.e.* the relative density of a-C12A7 film is 100% (2.9 gcm^{-3}) and there is no water-containing nanopores in the film).[27] The TFT characteristics at RT with the results of CAN-gated VO_2 TFT are summarized in Supporting Information Fig. S5. The I_g for dry a-C12A7-gated VO_2 TFT was <1 nA at most, which is ~10^6 times smaller than that of CAN-gated VO_2 TFT, indicating that pure electric field effect is dominant. Although the C of 210 pF for a-C12A7 film is higher than that (160 pF) of CAN film,[20] both the R_s and S-values have kept almost unchanged even at V_g = +40 V (The maximum R_s modulation ratio was ~0.1%). The MI phase conversion by

electric-field effect was not observed in dry a-C12A7-gated VO_2 TFTs and should originate from water-electrolysis in the CAN gate insulator.

To further confirm that the metallization of VO_2 based water-electrolysis TFTs originates from protonation rather than the formation of oxygen vacancies,[15] the protonated TFT was heated in a vacuum. Annealing temperature dependence of R_s for the protonated TFTs, measured at RT, is shown in Figure S4b in Supporting Information. R_s was nearly constant at annealing temperatures below 100 °C, but significantly increased at 150 °C and R_s returned to the insulating state. These observations indicate that thermal deprotonation of H_xVO_2 occurred at 150 °C, which is consistent with the result for bulk H_xVO_2 (87 °C[18]). The increase of R_s in the TFTs upon heating in a vacuum supports that the device operation does not originate from the formation of oxygen vacancies.

Additionally, protonation of VO_2 TFTs is further supported by the change of ED patterns on electron beam irradiation (Figure S6 in Supporting Information for ED patterns of the protonated VO_2 TFTs as a function of irradiation time of electron beam). The ED patterns of protonated VO_2 films changed and the diffraction spots of superstructures appeared as the irradiation time (t) increased, where the ED pattern of VO_2 TFTs at t = 90 sec can correspond to M2-type monoclinic structure.[28] These observations indicate that the tetragonal structure (metal) changed to monoclinic structure (insulator) upon electron beam irradiation at RT, which can be explained if thermal deprotonation occurs in a vacuum. A similar result was observed for p-type GaN:Mg thin films grown by MOCVD[29,30]; the obstacle hydrogen produced by NH_3 dissociation can be removed from GaN:Mg film by electron beam irradiation in a vacuum and accordingly p-type conduction was realized. Although it is difficult to completely rule out the contribution of oxygen vacancies,,these results should support the water-electrolysis-induced protonation of VO_2 film at RT.

In summary, we demonstrated a new solid-state device for water-electrolysis-induced

protonation and nonvolatile and reversible switching of metal-insulator conversion of VO_2 at RT. We fabricated a transistor structure on an insulating VO_2 thin film using water-infiltrated nanoporous glass (CAN) as a solid gate insulator, which acts as a solid electrolyte. A gate voltage application induced water electrolysis in the CAN gate insulator with large ion current *i.e.*, nanosized electrochemical cell, and the produced protons were effectively incorporated and removed from VO_2 film, which results in a highly reversible alternation of the electronic state from an insulator to a metal. The reversible protonation clearly accompanied a change in the VO_2 crystal structure from insulating monoclinic to metal tetragonal phase. These findings provide a new pathway to realize all-solid-state electrochromic devices based on VO_2 for energy-saving applications that reversibly change the infrared transmission, while maintaining the visible-light transparency. At this stage, the modulation thickness is limited to be ~10 nm because the electric field is terminated at a thin layer of VO_2 channel and protons cannot penetrate deeper into insulating VO_2 layer. Indeed, it is difficult to apply this TFT structure to optical devices because, for practical use, a large change in transmittance is required and thus thicker film should be used. We consider that the all-solid state electrochromic device can be practical by changing the device structure to sandwich-type construction (*e.g.* ITO top electrode / CAN gate insulator /VO_2 film / SnO_2:F bottom electrode) on glass substrate, where the electric field can be applied over the thickness of VO_2 layer and the optical properties is largely modulated by RT protonation. The present approach should lead to the development of electro-optically active solid-state devices with TMO materials by engineering RT-protonation.

Experimental section

Device Fabrication: TFT structures (Figure1a) were fabricated on 20 nm-thick VO_2 epitaxial films using metal shadow masks. The dimensions of the channel were 400 μm in width and 800 μm in length. The VO_2 channel layer was grown at 500 ºC under O_2 pressure (P_{O2}) of 2.0

Pa on $(11\bar{2}0)$ α-Al_2O_3 substrates (10 × 10 × 0.5 mm^3) by pulsed laser deposition (PLD). A KrF excimer laser (wavelength of 248 nm) was used to ablate a V_2O_5 polycrystalline target disk, where the laser energy fluence and the repetition rate were 3 J cm^{-2} $pulse^{-1}$ and 10 Hz, respectively. Afterwards the films were cooled to RT under the same oxygen pressure. The VO_2 film with a monoclinic structure was heteroepitaxially grown on α-Al_2O_3 substrate with an epitaxial relationship of $(100)[010]VO_2 \parallel (11\bar{2}0)[0001]\alpha\text{-}Al_2O_3$, which was confirmed by high-resolution XRD at RT (Figure S1 in Supporting Information). Second, 20-nm-thick metallic Ti films, which served as both the source and drain electrodes, were deposited by e-beam (EB) evaporation in a vacuum (~10^{-4} Pa, no substrate heating). Then, 200-nm-thick CAN gate insulator was deposited by PLD (KrF excimer laser with energy fluence of 3 J cm^{-2} $pulse^{-1}$) at RT under P_{O2} of 5 Pa to make CAN film nanoporous structure.[20] The bulk density of the resultant CAN film was 2.07 g cm^{-3}, evaluated by grazing incidence X-ray reflectivity, which corresponds to 71 % of fully dense amorphous C12A7 glass (2.92 g cm^{-3}). [20] AC conductivity of the CAN film was 3.7 × 10^{-8} S cm^{-1} at RT, which was slightly smaller than 5.6 × 10^{-8} S cm^{-1} of ultrapure water. Finally, a 50-nm-thick metallic Ti film, used as the gate electrode, was deposited by EB evaporation at RT.

Electrical transport measurement: Gate current (I_g) was measured as a function of gate voltage (V_g) using a semiconductor device analyzer (B1500A, Agilent). Sheet resistance (R_s) was measured by d.c. four probe method in the van der Pauw electrode configuration. Thermopower (*S*-value) was measured by giving a temperature difference (ΔT) of ~4 K in the film using two Peltier devices while the actual temperatures of both sides of VO_2 film surface were monitored by two tiny thermocouples. The thermo-electromotive force (ΔV) and ΔT were simultaneously measured, and the *S*-values were obtained from the slope of the ΔV–ΔT plots. All the electrical property measurements were performed in an ambient atmosphere.

Structural analysis: TEM samples of the CAN-gated VO_2 TFTs were prepared by a focused-ion-beam (FIB) micro-sampling technique, in which the trilayer structure region of the TFTs was cutout and thinned by FIB (JIB-4600F, JEOL) to obtain samples for cross-sectional observation. The cross-sectional microstructure of VO_2 TFTs was examined at RT by HAADF-STEM (JEM-ARM200F, 200 kV, JEOL), where electron incident direction was sapphire [0001]. The ED patterns were observed by nanobeam electron diffraction with spot size of about 1.5 nm (JEM-2800, 200 kV, JEOL).

Acknowledgements
This work was supported by Grant-in-Aid for Scientific Research on Innovative Areas (25106007) from JSPS and Nanotechnology Platform Program (12024046) of MEXT. HO was supported by JSPS KAKENHI for Scientific Research A (25246023). TT was supported by JSPS KAKENHI for Young Scientists B (24760533) and the Network Joint Research Center for Materials and Devices.

[1] T. Norby, M. Widerøe, R. Glöckner, Y. Larring, *Dalton Trans.* **2004**, 19, 3012.

[2] A. Janotti, C. G. Van de Walle, *Nature Mater.* **2007**, 6, 44.

[3] C. G. Granqvist, *Handbook of Inorganic Electrochromic Materials*, Elsevier, Amsterdam, **1995**.

[4] C. Kilic, A. Zunger, *Appl. Phys. Lett.* **2002**, 81, 73.

[5] C. H. Ahn, J.-M. Triscone, J. Mannhart, *Nature* **2003**, 424, 1015.

[6] K. Ueno, S. Nakamura, H. Shomotani, A. Ohtomo, N. Kimura, T. Nojima, H. Aoki, Y. Iwasa, M. Kawasaki, *Nat. Mater.* **2008**, 7, 855.

[7] K. Vanheusden, W. L. Warren, R. A. B. Devine, D. M. Fleetwood, J. R. Schwank, M. R. Shaneyfelt, P. S. Winokur, Z. J. Lemnios, *Nature* **1997**, 386, 587.

[8] J. Yoon, W. Hong, M. Jo, G. Jo, M. Choe, W. Park, J. I. Sohn, S. Nedic, H. Hwang, M. E. Welland, T. Lee, *ACS Nano* **2011**, 5, 558.

[9] J. B. Goodenough, R. Manoharan, M. Paranthaman, *J. Am. Chem. Soc.* **1990**, 112, 2076.

[10] P. G. Dickens, S. J. Hibble, R. H. Jarman, *J. Electron. Mater.* **1981**, 10, 999.

[11] F. J. Morin, *Phys. Rev. Lett.* **1959**, 3, 34.

[12] J. B. Goodenough, *J. Solid State Chem.* **1971**, 3, 490.

[13] J. Wei, H. Ji, W. Guo, A. H. Nevidomskyy, D. Natelson, *Nature Nanotechnol.* **2012**, 7, 357.

[14] M. Nakano, K. Shibuya, D. Okuyama, T. Harano, S. Ono, M. Kawasaki, Y. Iwasa, Y. Tokura, *Nature* **2012**, 487, 459.

[15] J. Jeong, N. Aetukuri, T. Graf, T. D. Schladt, M. G. Samant, S. S. P. Parkin, *Science* **2013**, 339, 1402.

[16] T. Nan, M. Liu, W. Ren, Z-G. Ye, N. X. Sun, *Sci. Rep.* **2014**, 4, 5931.

[17] A. M. Chippindale, P. G. Dickens, A. V. Powell, *J. Solid State Chem.* **1991**, 93, 526.

[18] V. Andreev, V. Kapralova, V. Klimov, *Phys. Solid State* **2007**, 49, 2318.

[19] C. Wu, F. Feng, J. Feng, J. Dai, L. Peng, J. Zhao, J. Yang, C. Si, Z. Wu, Y. Xie, *J. Am. Chem. Soc.* **2011**, 133, 13798.

[20] H. Ohta, Y. Sato, T. Kato, S. W. Kim, K. Nomura, Y. Ikuhara, H. Hosono, *Nature Commun.* **2010**, 1, 118; H. Ohta, T. Mizuno, S. Zheng, T. Kato, Y. Ikuhara, K. Abe, H. Kumomi, K. Nomura, H. Hosono, *Adv. Mater.* **2012**, 24, 740.

[21] C. Ko, Z. Yang, S. Ramanathan, *ACS Appl. Mater. Interfaces* **2011**, 3, 3396.

[22] T. Katase, K. Endo, H. Ohta, *Phys. Rev. B* **2014**, 90, 161105(R).

[23] H. Ohta, S.-W. Kim, Y. Mune, T. Mizoguchi, K. Nomura, S. Ohta, T. Nomura, Y. Nakanishi, Y. Ikuhara, M. Hirano, H. Hosono, K. Koumoto, *Nature Mater.* **2007**, 6, 129.

[24] Y. Filinchuk, N. A. Tumanov, V. Ban, H. Ji, J. Wei, M. W. Swift, A. H. Nevidomskyy, D. Natelson, *J.Am. Chem. Soc.* **2014**, 136, 8100.

[25] J. Karel, C. E. ViolBarbosa, J. Kiss, J. Jeong, N. Aetukuri, M. G. Samant, X. Kozina, E. Ikenaga, G. H. Fecher, C. Felser, S. S. P. Parkin, *ACS Nano* **2014**, 8, 5784.

[26] R. D. Shannon, *Acta Cryst.* **1976**, A32, 751.

[27] H. Ohta, Y. Masuoka, R. Asahi, T. Kato, Y. Ikuhara, K. Nomura, H. Hosono, *Appl. Phys. Lett.* **2009**, 95, 113505.

[28] J. H. Park, J. M. Coy, T. S. Kasirga, C. Huang, Z. Fei, S. Hunter, D. H. Cobden, *Nature* **2013**, 500, 431.

[29] H. Amano, M. Kito, K. Hiramatsu, I. Akasaki, *Jpn. J. Appl. Phys.* **1989**, 28, L2114.

[30] S. Nakamura, N. Iwasa, M. Senoh, T. Mukai, *Jpn. J. Appl. Phys.* **1992**, 131, 1258.

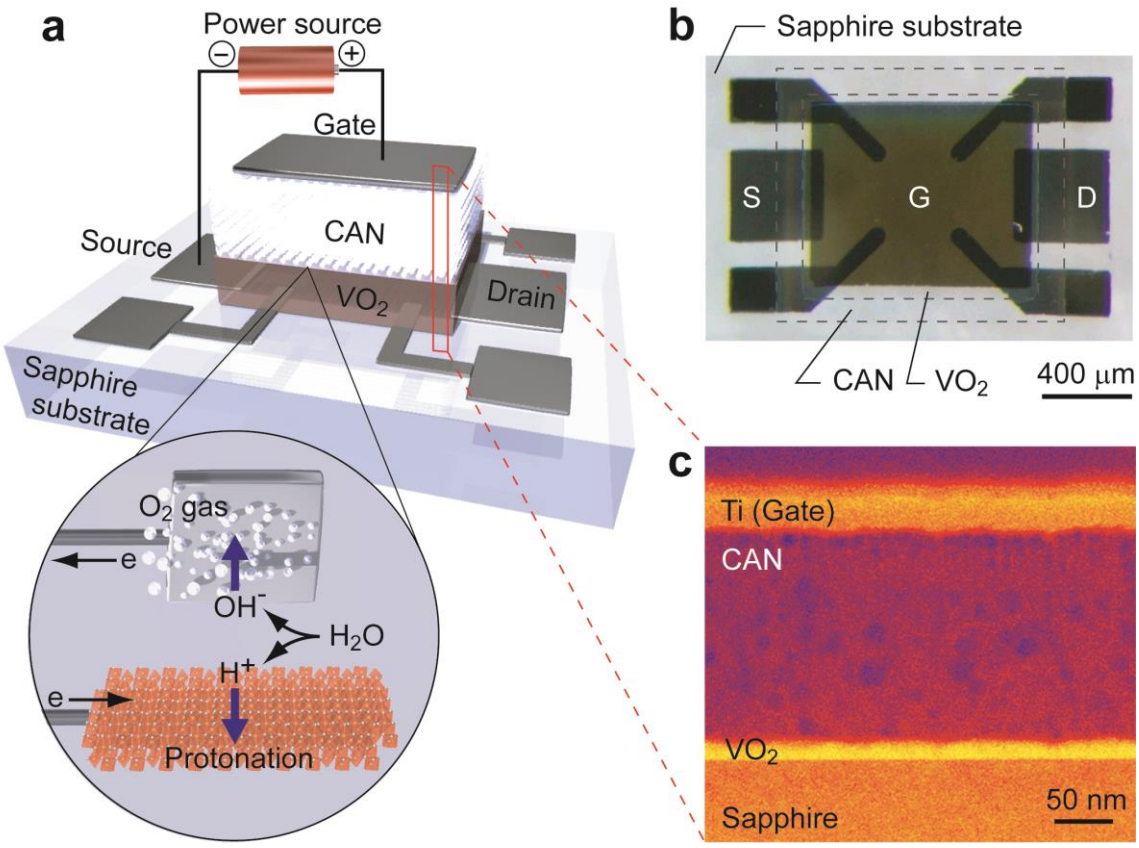

Figure 1. Water-electrolysis-induced protonation of VO_2 thin film. (a) Schematic of the thin film transistor (TFT) structure composed of Ti electrodes / water-infiltrated CAN gate insulator / VO_2 epitaxial film on sapphire substrate. Magnified image illustrates the principle of electrolysis-induced protonation of the VO_2 film. During positive gate voltage (V_g) application, H^+ and OH^- ions, which are produced by water electrolysis in the CAN film (nanosized electrochemical cell), move to the surfaces of VO_2 film and Ti gate electrode, respectively. H^+ ions penetrate into the VO_2 crystal (H_xVO_2) and OH^- ions become O_2 gas at each interface. (b) Optical micrograph of the VO_2-based TFT. Channel width and length are 400 μm and 800 μm, respectively. (c) Cross-sectional HAADF-STEM image of Ti (50 nm) / CAN (200 nm) / VO_2 (20 nm) / sapphire substrate. Nanopores with 10–20 nm diameters appear as dark contrasts in the CAN film.

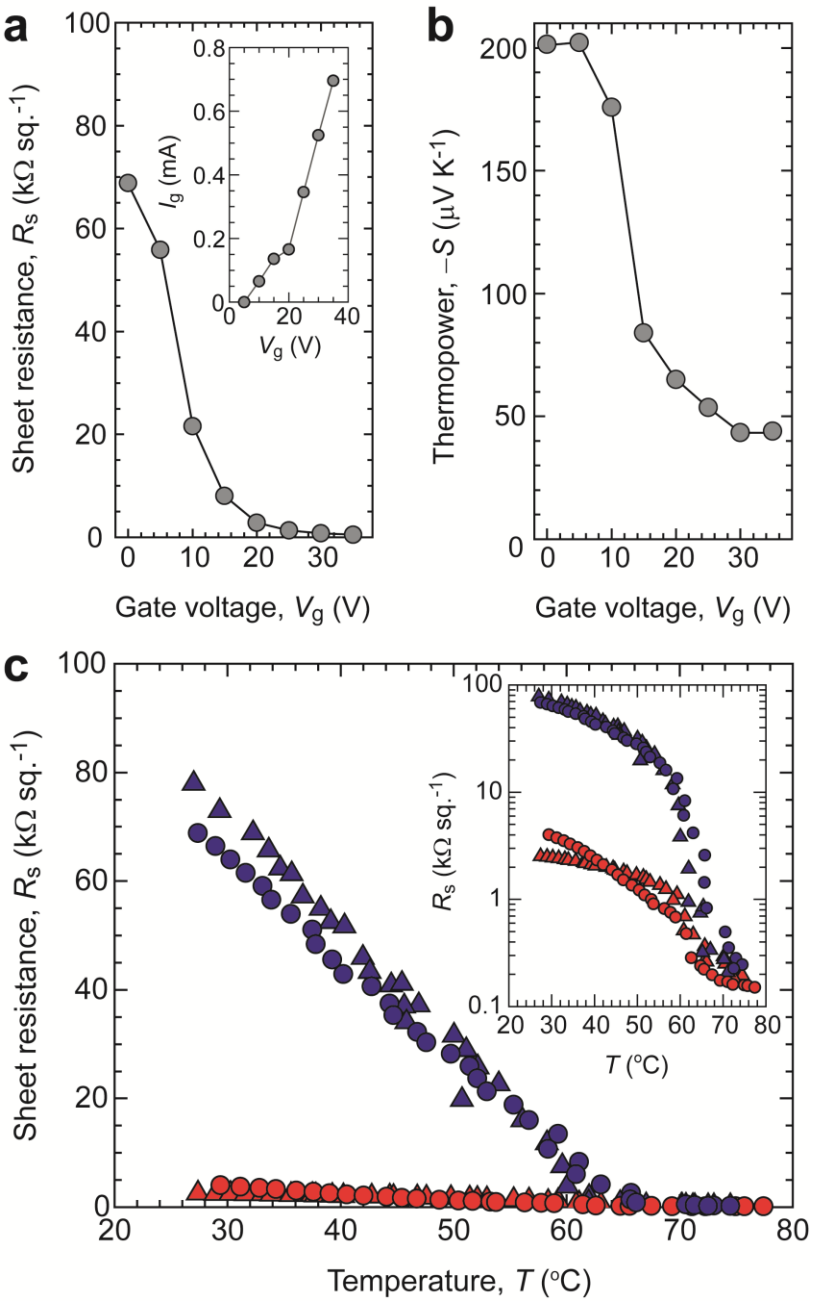

Figure 2. Protonation-driven metal-insulator conversion of VO_2 thin film. (a) Sheet resistance (R_s) as a function of V_g up to +35 V, where R_s was measured after holding the V_g application for 10 minutes. Inset shows V_g dependence of mean gate current (≡ion current, I_g) during the V_g application. I_g exponentially increased with $V_g \geq +10$ V due to water-electrolysis-induced protonation of VO_2. R_s simultaneously decreased with $V_g \geq +10$ V, indicating that the electronic state of VO_2 was altered from an insulator to a metal by water-electrolysis-induced

protonation. (b) Thermopower (S) as a function of V_g at RT. $|S|$ decreased with $V_g \geq +10$ V and was saturated at 43 μV K^{-1}, which is close to that of metallic H_xVO_2 (~35 μV K^{-1}).[19] (c) Temperature dependence of R_s measured before (blue closed circles) and after applying V_g alternately at +20 V (red closed symbols) and −20 V (blue closed triangles) at room temperature (RT). Each curve was measured after switching off the V_g. Inset shows logarithmic R_s vs. T. On/off ratio was ~30 at RT.

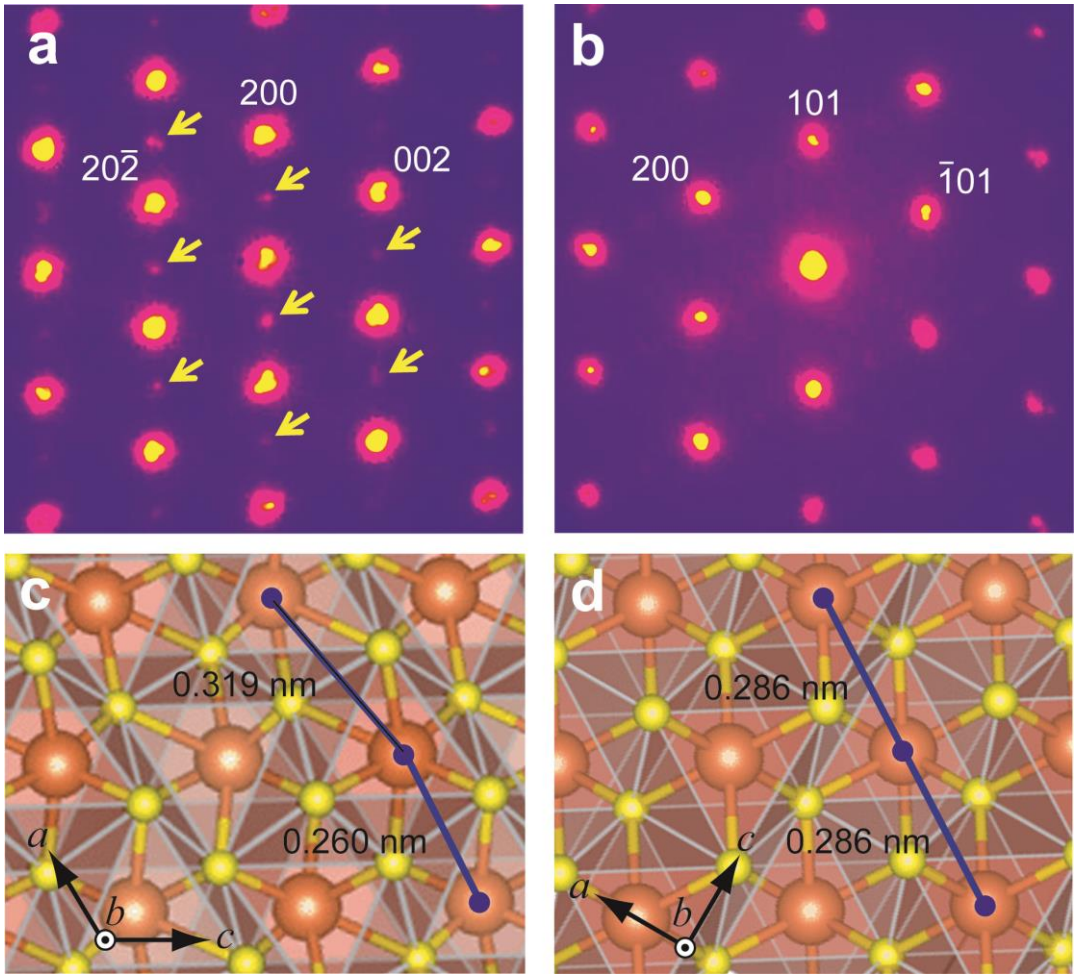

Figure 3 Structural analysis of protonated VO_2 thin film. Nano-beam electron diffraction patterns of (a) as-prepared and (b) protonated VO_2 films. The main diffraction indices are noted above the corresponding diffraction spots. Arrows in (a) indicate the diffraction spots due to vanadium-ion dimerization of monoclinic VO_2. Spots from the superstructure disappeared upon protonation (b), indicating the structural change from monoclinic to tetragonal phase. Schematic of the crystal structures for (c) monoclinic and (d) tetragonal phases. Brown and yellow denote vanadium and oxygen ions, respectively.

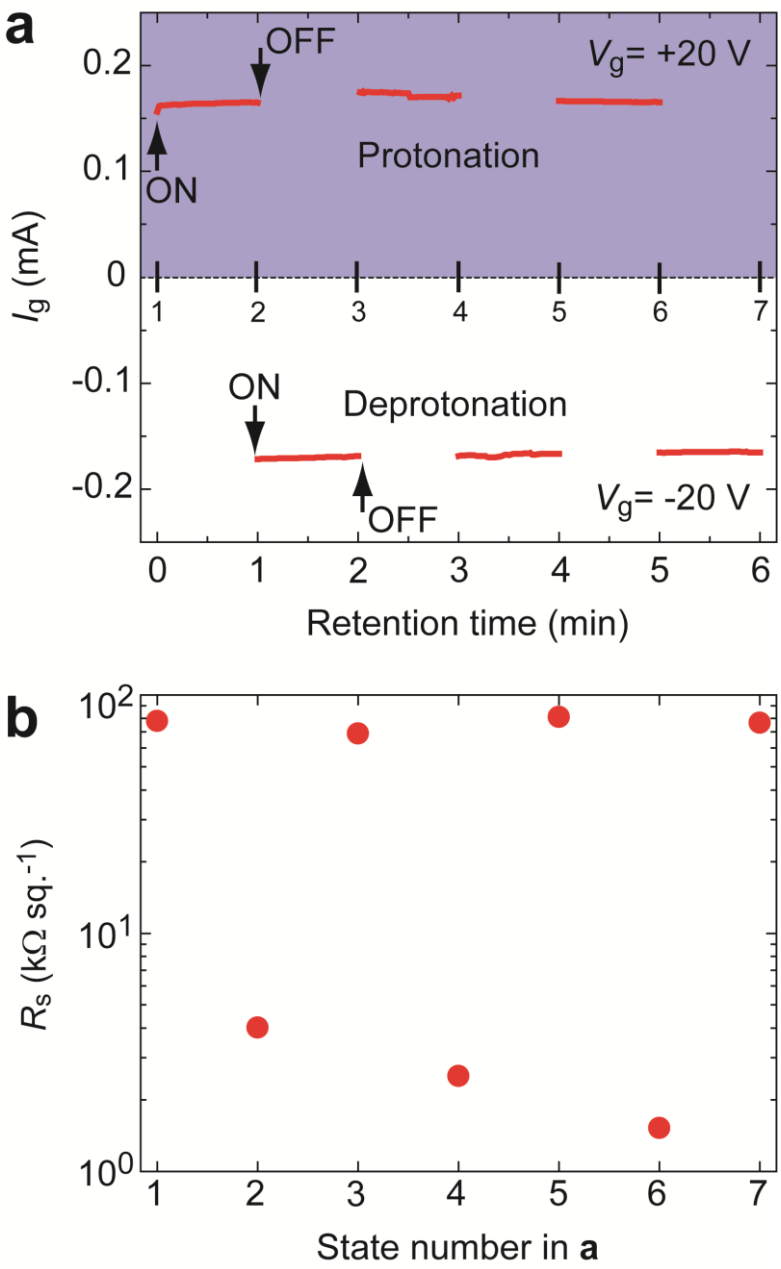

Figure 4 Reversible metal-insulator conversion of VO_2 thin film at room temperature. (a) Retention time dependence of I_g during the V_g application. VO_2 thin film was protonated at V_g= +20 V, whereas deprotonation occurs at V_g= −20 V. (b) R_s modulation at room temperature, which was measured for each state in (a).